



Impact of Cesium in Phase and Device Stability of Triple Cation Pb-Sn Double Halide Perovskite Films and Solar Cells

Journal:	<i>Journal of Materials Chemistry A</i>
Manuscript ID	TA-ART-07-2018-006391.R1
Article Type:	Paper
Date Submitted by the Author:	01-Aug-2018
Complete List of Authors:	Tosado, Gabriella; University of Washington, Chemical Engineering Lin, Yi-Yu; University of Washington Department of Chemical Engineering Zheng, Erjin; University of Washington, Chemical Engineering Yu, Qiuming; University of Washington, Chemical Engineering



Received 3th July 2018,

Impact of Cesium in Phase and Device Stability of Triple Cation Pb-Sn Double Halide Perovskite Films and Solar Cells

Gabriella A. Tosado,^a Yi-Yu Lin^a, Erjin Zheng^a and Qiuming Yu^a

Accepted 00th January 20xx

DOI: 10.1039/x0xx00000x

www.rsc.org/

Triple cation Cs/methylammonium (MA)/formamidinium (FA) and double halide Br/I lead perovskites improved the stability and efficiency of perovskite solar cells (PVSCs). However, their effects on alloyed Pb-Sn perovskites are unexplored. In this work, perovskite thin films with the composition $\text{Cs}_x(\text{MA}_{0.17}\text{FA}_{0.83})_{1-x}\text{Pb}_{1-y}\text{Sn}_y(\text{I}_{0.83}\text{Br}_{0.17})_3$ are synthesized utilizing a one-step solution process plus anti-solvent wash technique and deployed in PVSCs with an inverted architecture. All films show a cubic crystal structure, demonstrating that compositional tuning of both tolerance factor and crystallization rate allow for dense, single phase formation. The band gaps, affected by both lattice constriction and octahedral tilting, show opposite trends in Pb-rich or Sn-rich perovskites with the increase of Cs for fixed Sn compositions. The $\text{Cs}_{0.05}(\text{MA}_{0.17}\text{FA}_{0.83})_{0.95}\text{Pb}_{0.25}\text{Sn}_{0.75}(\text{I}_{0.83}\text{Br}_{0.17})_3$ PVSCs achieve the power conversion efficiency (PCE) of 11.05%, a record for any PVSC containing 75% Sn perovskites, and the $\text{Cs}_{0.10}(\text{MA}_{0.17}\text{FA}_{0.83})_{0.90}\text{Pb}_{0.75}\text{Sn}_{0.25}(\text{I}_{0.83}\text{Br}_{0.17})_3$ PVSCs reach a record PCE of 15.78%. Moreover, the triple cation and double halide alloyed Pb-Sn perovskites exhibit improved device stability in inert and ambient conditions. This study, which illustrates the impact of cation and halide tuning on alloyed Pb-Sn perovskites, can be used to further eliminate Pb and improve device performance on high Sn PVSCs and other optoelectronic devices.

Introduction

Hybrid organic-inorganic lead halide perovskite solar cells (PVSCs) have emerged in the past decade as a promising low-cost thin film photovoltaic device with power conversion efficiency (PCE) increasing from 3.8% to 22.7%.¹ The organic-inorganic perovskites follow a formula of AMX_3 , where A is a monovalent cation (e.g., methylammonium (MA^+ , CH_3NH_3^+), formamidinium (FA^+ , $\text{CH}_3(\text{NH}_2)_2^+$), and/or cesium (Cs^+)),² M is a divalent transition metal cation (e.g., Pb^{2+} and/or Sn^{2+}),³ and X is a halide anion (e.g., I, Br, and/or Cl).^{4,5} The intrinsic properties of perovskites, such as high absorption coefficient over the visible spectrum,⁶ long carrier diffusion length,⁷ low exciton binding energy,⁸ high carrier mobility,⁹ and a direct band gap,¹⁰ have contributed to high device performance.

Pure lead perovskites come with instabilities that have hindered PVSCs commercialization. Methylammonium based perovskites, such as MAPbI_3 , have thermal instabilities that result in the degradation of methylammonium and a phase transition from the preferred black cubic α -phase to a noncentrosymmetric dark brown tetragonal β -phase at 55°C.^{11,12} Due to the positive enthalpy of formation of MAPbI_3 , it easily

undergoes chemical reactions in ambient conditions and is degraded by water, oxygen, and light radiation, reverting the perovskite back to its precursors.^{13,14} Although the cubic α -phase FAPbI_3 is thermally stable at high temperatures and can lead to more efficient solar cells, due to a lower band gap of 1.48 eV compared to that of 1.61 eV of MAPbI_3 , it is still sensitive to humidity and undergoes a phase transition to a tetragonal β -phase at room temperature, and also to a yellow photoinactive hexagonal δ -phase.¹² CsPbI_3 has been studied as an all-inorganic option for PVSCs to avoid the sensitivity to heat and humidity that is common in organic cation devices. Unfortunately, CsPbI_3 perovskites phase change from the favourable cubic α -phase to a yellow photoinactive hexagonal δ -phase at room temperature. This undesirable phase transition is due to the smaller radius of Cs^+ (1.67 Å) being unable to support the PbI_6 octahedral frame necessary for a cubic crystal lattice.^{15,16} Replacing I with the smaller Br has been shown to shrink this octahedral frame enough to stabilize the cubic α -phase, but this replacement tunes the band gap to 2.3 eV, making it unable to absorb long wavelength light, resulting in low PCE.¹⁷

To improve phase stability while also tuning the band gap, Snaith and co-workers partially replaced FA^+ with Cs^+ in mixed halide perovskites $\text{FAPb}(\text{I}_{1-z}\text{Br}_z)_3$, creating the cubic structure for all Br compositions tested with band gaps ranging from 1.48 to 2.3 eV. The $\text{FA}_{0.83}\text{Cs}_{0.17}\text{Pb}(\text{I}_{0.6}\text{Br}_{0.4})_3$ single junction solar cell reached a maximum PCE of 17.1%.¹⁸ The high efficiencies for single-junction PVSCs have also been achieved by optimizing the compositions of the A- and X- sites of perovskites (such as FAI_3

^a Department of Chemical Engineering, University of Washington, Seattle, WA 98195, USA

Electronic Supplementary Information (ESI) available: [details of any supplementary information available should be included here]. See DOI: 10.1039/x0xx00000x

ARTICLE

Journal of Materials Chemistry A

$x\text{MA}_x\text{Pb}(\text{I}_{1-y}\text{Br}_y)$. Graetzel and co-workers were able to consistently achieve > 20% PCE for the PVSCs with the $(\text{MA}_{0.17}\text{FA}_{0.83})\text{Pb}(\text{I}_{0.83}\text{Br}_{0.17})_3$ perovskites. By mixing $(\text{MAPbBr}_3)_{0.17}$ with $(\text{FAPbI}_3)_{0.83}$, it can slow the crystallization process, creating smoother, reproducible films. The improved band alignment led to record short-circuit current densities.^{19,20} Graetzel's group further introduced Cs to the A-site and demonstrated a device performance of 21.1% PCE with improved stability in ambient conditions for the $\text{Cs}_{0.05}(\text{MA}_{0.17}\text{FA}_{0.83})_{0.95}\text{Pb}(\text{I}_{0.83}\text{Br}_{0.17})_3$ PVSCs, which was attributed to the smaller Cs^+ (1.67 Å) and MA^+ (2.16 Å) ions "pushing" the larger FA^+ (2.53 Å) ion into the black cubic α -phase.² Li and co-workers conducted the solvent engineering study using $\text{Cs}_{0.05}(\text{MA}_{0.17}\text{FA}_{0.83})_{0.95}\text{Pb}(\text{I}_{0.83}\text{Br}_{0.17})_3$ perovskites and reiterated the improved stability, performance, and reproducibility of the PVSCs by adding a small amount of Cs^+ .²¹ It is thus imperative to design mix cation and halide perovskites to improve device stability.

To reduce environmental toxicity of lead based PVSCs, tin was investigated as a replacement due to its similar electronic configuration as a group 14 metal and the ability to form a MX_6 octahedron necessary for the cubic structure.²² The comparable ionic radius, Sn^{2+} (1.15 Å) and Pb^{2+} (1.19 Å), allows for minimized tolerance factor differences, optimizing cubic α -phase stability.²³ Sn-based perovskites also have the benefit of lower band gaps by forming Pb-Sn binary alloyed perovskites, such as $\text{MAPb}_{0.3}\text{Sn}_{0.7}\text{I}_3$ that reaches the minimum band gap of 1.17 eV.^{24,25,26} Combining the transition metal tuning with the halide tuning has recently created an ideal band gap of 1.35 eV for $\text{MAPb}_{0.5}\text{Sn}_{0.5}(\text{I}_{0.8}\text{Br}_{0.2})_3$ perovskites that can lead to a theoretical Shockley Queisser efficiency of 33%.²⁷ Unfortunately, crystallization and stability of high Sn-containing perovskites have impeded the progress of Sn-based PVSCs. The reaction between MAI and SnI_2 is recognized to be faster than PbI_2 due to the greater Lewis acidity of Sn^{2+} versus Pb^{2+} , resulting in uncontrollable crystallization during solution processing.²⁸ MASnI_3 perovskites are, therefore, prone to poor film coverage with micron sized pinholes limiting device performance without solvent or deposition engineering. Kanatzidis and co-workers obtained pinhole-free MASnI_3 perovskite films using N,N-dimethyl sulfoxide (DMSO) solvent to form $\text{SnI}_2 \cdot 3\text{DMSO}$ complex intermediate phase. This intermediate phase allows the MA^+ ions to react with SnI_2 in a controlled manner where the rate-limiting step is the removal of DMSO through thermal annealing. The corresponding devices achieved a short circuit current density (J_{sc}) of 21.4 mA cm^{-2} .²⁹ Jen and co-workers developed a one-step solution thin film formation method using γ -butyrolactone (GBL):DMSO co-solvents to dissolve precursors combined with an anti-solvent toluene wash step to further control crystallization rates, which resulted in pinhole-free perovskite films and allowed for high performance of $\text{MA}_{0.5}\text{FA}_{0.5}\text{Pb}_{0.75}\text{Sn}_{0.25}\text{I}_3$ PVSCs reaching a PCE of 14.19%.³⁰ Sn-containing PVSCs also have been shown to degrade from the oxidation of Sn^{2+} to the more thermodynamically favoured Sn^{4+} , even in inert atmospheres, due to the small formation energy and relatively weak inert pair effects.²⁸ The high levels of self-p-

doping caused by Sn^{4+} limit the diffusion length for charge carriers. To reduce the oxidation of Sn^{2+} , SnF_2 was first added in making CsSnI_3 perovskite thin films to fill Sn vacancies with extra Sn^{2+} ions, suppressing Sn^{4+} centers as well as reducing Sn^{4+} back to a divalent metal.^{31,32} Attempts have since been made to utilize SnF_2 as a reducing agent to improve the performance of high Sn PVSCs. Seok *et al.* used a pyrazine- SnF_2 complex to reduce Sn^{2+} oxidation and slow crystallization of FASnI_3 perovskites and demonstrated a PCE of 4.8%.³³ Yan *et al.* later reported a record efficiency of 6.22% for FASnI_3 using SnF_2 as a reducing agent on a p-i-n planar solar architecture.³⁴ The introduction of Cs has also been shown to reduce the crystallization rate and improve the stability of compositions $\text{MAPb}_{0.5}\text{Sn}_{0.5}\text{I}_3$, and $\text{FAPb}_{1-x}\text{Sn}_x\text{I}_3$. Jen and co-workers showed that a 10% Cs addition improved the stability of $\text{MA}_{0.9}\text{Cs}_{0.1}\text{Pb}_{0.5}\text{Sn}_{0.5}\text{I}_3$ perovskites allowing for pristine, unencapsulated devices to retain 75% of initial PCE after 12 days in inert conditions and 76% of initial PCE after 20 days in ambient conditions.²⁴

This gives rise to our strategy of using triple Cs/MA/FA cation with mixed Br/I halide to stabilize high Sn PVSCs. In this work, we combined compositional tolerance factor tuning and solvent-washing methodology to create the first reproduction of cubic α -phase, homogeneous and densely packed polycrystalline $\text{Cs}_x(\text{MA}_{0.17}\text{FA}_{0.83})_{1-x}\text{Pb}_{1-y}\text{Sn}_y(\text{I}_{0.83}\text{Br}_{0.17})_3$ films with $x = 0.05, 0.10,$ and 0.20 and $y = 0, 0.25, 0.50, 0.75,$ and 1.0 . To improve general device stability, we used a simple inverted device structure of indium tin oxide (ITO)/poly (3,4, -ethylenedioxythiophene): polystyrene sulfonate (PEDOT:PSS)/Perovskite/[6,6]-phenyl- C_{60} -butyric acid methyl ester (PC_{60}BM)/fullerene (C_{60})/2,9-dimethyl-7,7-diphenyl-1,10-phenanthroline (BCP)/Ag. This solar cell architecture eliminated the need for dopants that introduce instabilities and decreased hysteresis, allowing stable maximum powers. Due to the high-quality film morphology and ideal single junction band gap (1.36 eV) of $\text{Cs}_{0.10}(\text{MA}_{0.17}\text{FA}_{0.83})_{0.9}\text{Pb}_{0.75}\text{Sn}_{0.25}(\text{I}_{0.83}\text{Br}_{0.17})_3$, the derived PVSCs reached a maximum PCE of 15.78%. The triple cation mixture and SnF_2 additive alleviated Sn oxidation for $\text{Cs}_{0.05}(\text{MA}_{0.17}\text{FA}_{0.83})_{0.95}\text{Pb}_{0.25}\text{Sn}_{0.75}(\text{I}_{0.83}\text{Br}_{0.17})_3$ (band gap = 1.30 eV), resulting in a record maximum PCE of 11.05% for the corresponding PVSC. Moreover, the 75% Sn PVSCs can retain 80% of initial PCE after 30 days storage in inert conditions followed by over 100 hours in ambient conditions. The triple cation Pb-Sn double halide perovskites not only offer a wide tunability on band gap to achieve ideal band gaps for single-junction or tandem PVSCs but also greatly improve the performance and stability of high Sn PVSCs, leading to the possibility to achieve stable, high efficiency lead-free devices.

Results and discussion

To achieve good film morphology, we used the one-step solution process and optimized anti-solvent engineering to synthesize dense, pinhole-free perovskite thin films. All precursors (MAI, FAI, PbI_2 , PbBr_2 , and FABr) were dissolved in a DMSO:GBL (3:7, v/v) co-solvent to a total concentration of 2.5 M. 10% mol SnF_2

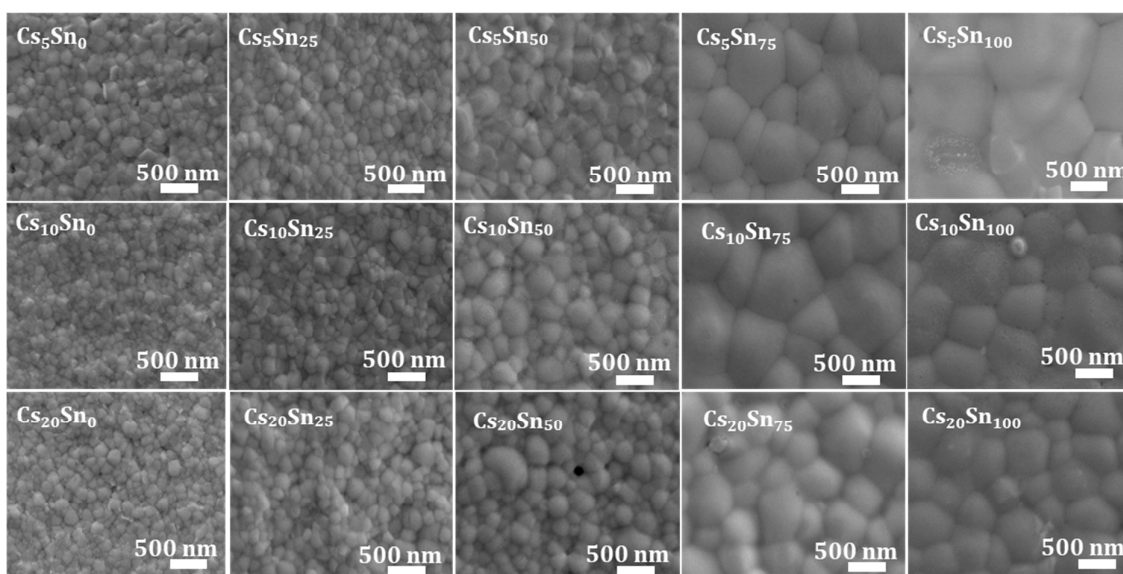


Fig 1. SEM images of $\text{Cs}_x(\text{MA}_{0.17}\text{FA}_{0.83})_{1-x}\text{Pb}_{1-y}\text{Sn}_y(\text{I}_{0.83}\text{Br}_{0.17})_3$ perovskite thin films with $x = 0.05, 0.1$ and 0.2 and $y = 0, 0.25, 0.50, 0.75$ and 1.0 .

with respect to Sn content was added to suppress the formation of Sn^{4+} . During spin coating, the anti-solvent wash with toluene was performed to remove excess DMSO from the complexes $\text{PbI}_2\cdot 2\text{DMSO}$ and $\text{SnI}_2\cdot 3\text{DMSO}$ to create the rapid formation of A-PbI₂-DMSO and A-SnI₂-2DMSO intermediates. It has been previously shown that the PbI₂-DMSO complexes yield an expanded lattice compared to neat PbI₂. This volume expansion facilitates the intramolecular exchange processing due to the volatility of the DMSO molecules in this adduct structure.³⁵ One SnI₂ forms a complex with 3 DMSO in the precursor solution due to the high bond energy of Sn-O (528 kJ mol⁻¹) compared to that of Pb-O (374 kJ mol⁻¹) supporting the preferential attachment of DMSO to Sn.³⁶ In our previous work, we demonstrated the role of DMSO in enhancing MAPb_{1-x}Sn_xI₃ and MAPbCl₃ film morphology and crystallinity.^{37,38} The volume of toluene was decreased with increased Sn percentage and amount of complexes SnI₂·3DMSO to minimize multiple DMSO removal from the complexes before annealing. Multiple DMSO removals would create A-SnI₂-DMSO instead of A-SnI₂-2DMSO intermediates, hindering the slower controlled removal of DMSO and reaction upon annealing, resulting in pinholes. All the films, except those of 100% Sn, were annealed at 100°C for 10 min to remove complexed DMSO under a controlled reaction of metal and cation during the annealing step, creating homogeneous, densely packed Pb-Sn perovskite films with clear grain boundaries. Films with 10 and 20 % Cs and pure Sn were found to have better morphology when annealed at 110°C, most likely due to the stronger bond in the A-SnI₂-2DMSO complex, which would require a higher temperature to break.

Fig. 1 shows the scanning electron microscopy (SEM) images of the perovskite thin films with the compositions of $\text{Cs}_x(\text{MA}_{0.17}\text{FA}_{0.83})_{1-x}\text{Pb}_{1-y}\text{Sn}_y(\text{I}_{0.83}\text{Br}_{0.17})_3$, where $x = 0.05, 0.1$, and 0.2 and $y = 0, 0.25, 0.50, 0.75$, and 1.0 . The low magnification SEM images are shown in **Fig. S1** to demonstrate the film quality and quantify the average grain sizes. To make description simple, we will use the notation Cs_xSn_y to represent the thin

films. For example, $\text{Cs}_5\text{Sn}_{25}$ represents the thin films with the composition of $\text{Cs}_{0.05}(\text{MA}_{0.17}\text{FA}_{0.83})_{0.95}\text{Pb}_{0.75}\text{Sn}_{0.25}(\text{I}_{0.83}\text{Br}_{0.17})_3$. As shown in **Fig. 1**, for each Cs composition, the grain size increased slightly with the addition of Sn to 50%. A notable grain size increase was observed when the Sn composition was greater than 50%. This could be due to the higher coordination of DMSO to Sn (A-SnI₂-2DMSO) compared to Pb (A-PbI₂-DMSO) formed for high Sn composition intermediates, allowing for even slower crystallization upon annealing as one mole of DMSO is first removed (A-SnI₂-DMSO) followed by the second, thus leading to larger grains. Sn addition has been shown to increase grain size with large grains for high Sn perovskites.³² For each Sn composition, Cs addition had no notable changes in grain size. The large area SEM images (**Fig. S1**) shows that pinhole-free films were formed for all Cs compositions with 50% Sn or lower. Smooth, dense, pinhole-free morphologies were also formed for the $\text{Cs}_5\text{Sn}_{75}$ and $\text{Cs}_{10}\text{Sn}_{75}$ films while obvious pinholes were formed in the $\text{Cs}_{20}\text{Sn}_{75}$ film. The $\text{Cs}_5\text{Sn}_{100}$ film has the largest, most prominent pinholes as well as an amorphous phase around the grain boundaries with a poor morphology apparent in **Fig. S1** while both $\text{Cs}_{10}\text{Sn}_{100}$ and $\text{Cs}_{20}\text{Sn}_{100}$ films have a few, small pinholes and more even coverage. A few smaller, lighter grains appeared in the $\text{Cs}_{10}\text{Sn}_{100}$ and $\text{Cs}_{20}\text{Sn}_{100}$ films, which could be due to a slight phase segregation.

The thin films were further characterized with X-ray diffraction (XRD) to determine the phase and crystallinity. As shown in **Fig. 2a**, all thin films have a cubic α -phase with the Pm-3m space group. The absence of additional peaks, such as the photoinactive hexagonal δ -phase FAPbI_3 at 11.63°, the orthorhombic δ -phase CsPbI_3 at 9.80° and 13.00°, the unreacted, cubic PbI_2 at 12.85°, and the tetragonal perovskite peaks indicated by the asterisk symbol, confirms the pure crystalline phase of the synthesized perovskite films.^{34,39,40} The strong diffraction from the (100) and (200) planes indicates a favourable orientation with the glass substrate. The shifts of the (100) diffraction peak for all synthesized perovskite films are

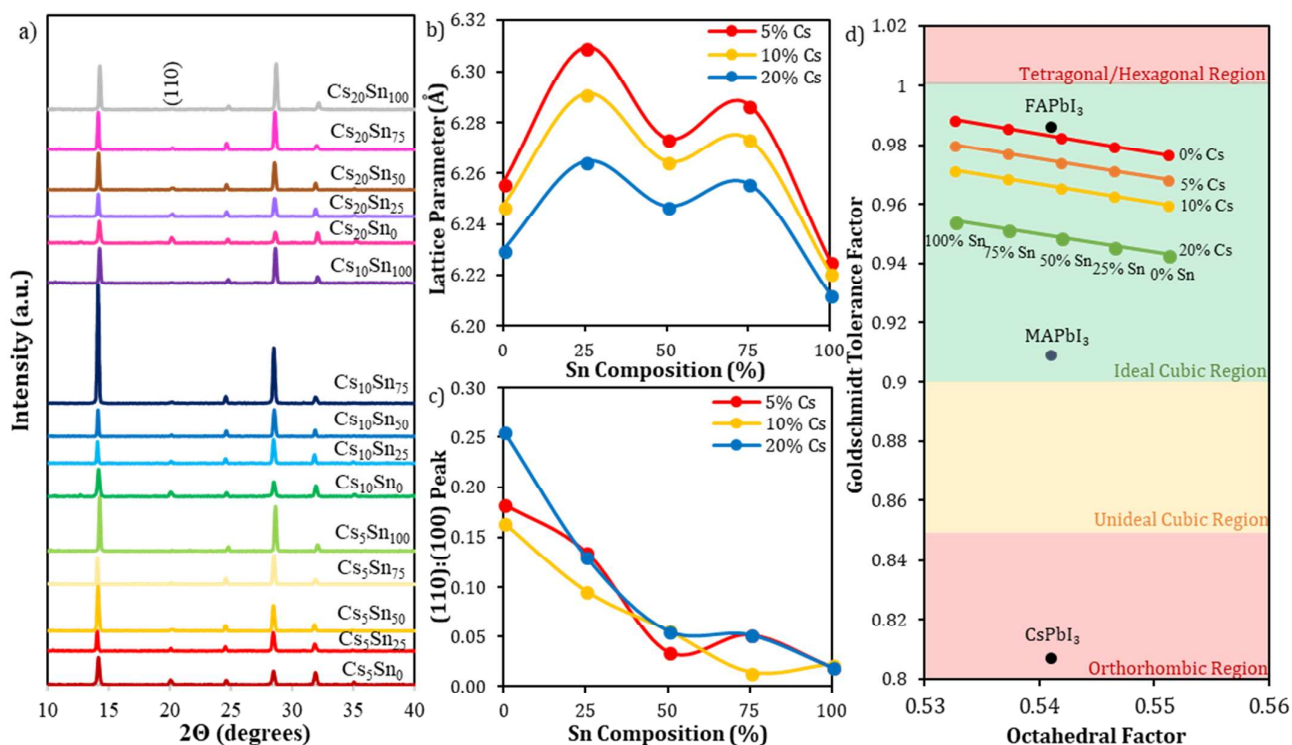


Fig. 2. a) X-ray diffraction (XRD) patterns of $\text{Cs}_x(\text{MA}_{0.17}\text{FA}_{0.83})_{1-x}\text{Pb}_{1-y}\text{Sn}_y(\text{I}_{0.83}\text{Br}_{0.17})_3$ perovskite thin films with $x = 0.05, 0.1$ and 0.2 and $y = 0, 0.25, 0.50, 0.75$ and 1.0 . b) The cubic lattice parameters as a function of Sn composition for each Cs composition of all perovskites. The inset shows the lattice parameter versus Cs composition for each Sn composition. c) The intensity ratio of the (110) and (100) peaks ($I_{(110)}/I_{(100)}$) as a function of Sn composition for each Cs composition of all perovskites. d) Goldschmidt tolerance factor calculations for corresponding compositions with phase change regions.

clearly shown in **Fig. S2**. For increasing Cs with a fixed Sn, the (100) peak right shifts (Fig. S2a), resulting in a reduced lattice parameter (Fig. 2b) because of the incorporation of the smaller Cs ion ($r = 1.67 \text{ \AA}$), supporting the successful incorporation of Cs.^{41,42} **Fig. 2d** illustrates that the incorporation of the smaller Cs ion pushes the Goldschmidt tolerance factor into a more cubic region for all Sn compositions and further from the hexagonal region, which stabilizes the perovskites against unwanted phase changes. The addition of Cs was also used to further optimize the Goldschmidt tolerance factor (GTF) of the perovskite compositions. GTF was first used for metal-oxide perovskites and has been applied to metal-halide perovskites as a way to quasi-quantify the stability of various composition perovskites.^{15,43} The GTF of a 3D cubic ABX_3 perovskite is represented by:

$$\text{GTF} = \frac{(r_A + r_X)}{\sqrt{2}(r_B + r_X)}$$

where r_A , r_B and r_X are the ionic radii of the monovalent cation, divalent transition metal cation, and halide anion, respectively. The radii of MA^+ (2.16 \AA), FA^+ (2.53 \AA), Cs^+ (1.67 \AA), Pb^{2+} (1.19 \AA), Sn^{2+} (1.15 \AA), I^- (2.20 \AA), and Br^- (1.96 \AA) were used to calculate the GTFs of all perovskites.⁴⁴ The octahedral factor (μ) is another quantifying ratio of divalent transitional metal cation radius to halide anion radius (r_B/r_X). Stable cubic α -phase perovskites are expected to exhibit a GTF between 0.8 to 1 and an octahedral factor, μ , between 0.44 and 0.90.⁴⁵ Experimentally,

perovskites are more stable when GTF is between 0.9 and 1 and $\text{GTF} > 1$ enters the hexagonal/tetragonal phase and $\text{GTF} < 0.8$ enters the orthorhombic phase. The GTFs and octahedral factors of $\text{Cs}_x(\text{MA}_{0.17}\text{FA}_{0.83})_{1-x}\text{Pb}_{1-y}\text{Sn}_y(\text{I}_{0.83}\text{Br}_{0.17})_3$ perovskites with $x = 0, 0.05, 0.1$ and 0.2 and $y = 0, 0.25, 0.5, 0.75$ and 1 are graphed in Figure S3. In addition, these factors of CsPbI_3 , MAPbI_3 and FAPbI_3 are also marked in the graph. As shown in Fig. 2d, all perovskites tested fall in the cubic phase range of octahedral factor. GTF is shown to increase with the increasing of Sn composition and decreases with the increasing of Cs composition. MAPbI_3 and FAPbI_3 are at the lower and higher boundary of the GTF region for ideal cubic phase, respectively. Even though the tolerance factor of α - FAPbI_3 is 0.986 calculated based on the radius of FA^+ (2.53 \AA), the non-sphericity of FA^+ complicates the calculation, making an actual tolerance factor around 1.03.⁴⁶ This tolerance factor borders on the hexagonal region ($\text{GTF} > 1$) at room temperature, explaining the instabilities of α - FAPbI_3 . Adding MA and Br to form $(\text{MA}_{0.17}\text{FA}_{0.83})\text{Pb}(\text{I}_{0.83}\text{Br}_{0.17})_3$ (i.e., Cs_0Sn_0) allows for a smaller tolerance factor (0.977) moving more into the cubic phase region. However, forming Pb-Sn alloy perovskites based on this mixed MA/FA and I/Br formula lead to increased GTFs with increasing Sn contents. $\text{Cs}_0\text{Sn}_{100}$ reaches a GTF of 0.989, exceeding than that of FAPbI_3 . Introducing Cs can decrease GTFs, allowing for even pure Sn perovskites to have a more cubic tolerance. For example, adding 5, 10 and 20 % Cs, i.e., $\text{Cs}_5\text{Sn}_{100}$,

$\text{Cs}_{10}\text{Sn}_{100}$ and $\text{Cs}_{20}\text{Sn}_{100}$, decrease the GTFs to 0.980, 0.972 and 0.954, respectively. The lower GTFs indicate that introducing Cs can entropically stabilize the perovskites at room temperature, likely leading to higher stabilities. This is in good agreement with previous reports of triple cation mixture for tolerance tuning.^{15,41,47} Using the three-cation mixture also alleviates the size mismatch of Cs and FA, decreasing the chance for entropic phase separation.

compositions, there is a significant decrease in the (110) and (111) peaks showing a more preferred orientation of the (100) plane.

The UV-Vis absorption spectra of the $\text{Cs}_x(\text{MA}_{0.17}\text{FA}_{0.83})_{1-x}\text{Pb}_{1-y}\text{Sn}_y(\text{I}_{0.83}\text{Br}_{0.17})_3$ perovskite thin films are shown in Fig. S3a-c. As the incorporation of Sn was increased to 100%, the absorption spectra showed a softened band edge due to sub-band gap states and scattering, making it difficult to determine the band gap.

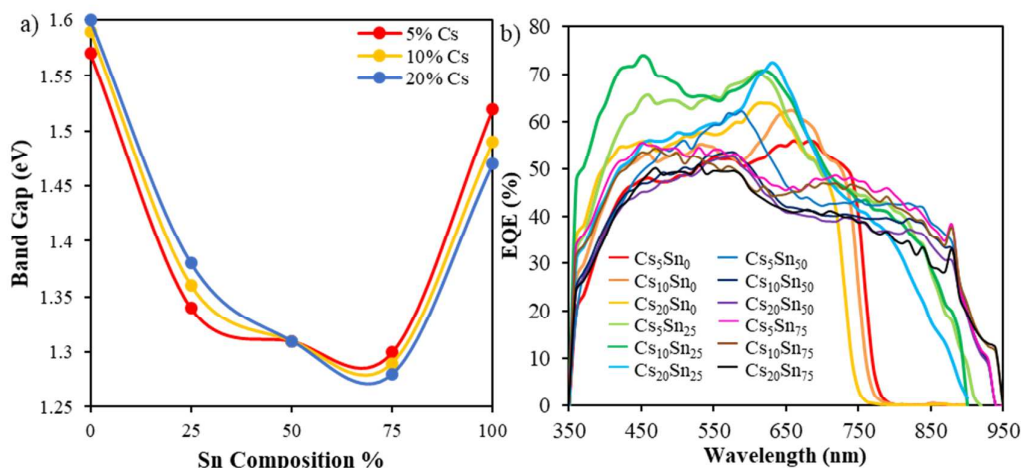


Fig. 3. a) The band gap of $\text{Cs}_x(\text{MA}_{0.17}\text{FA}_{0.83})_{1-x}\text{Pb}_{1-y}\text{Sn}_y(\text{I}_{0.83}\text{Br}_{0.17})_3$ perovskite thin films as a function of Sn composition for different Cs contents. b) The EQE spectra of PVSCs with the $\text{Cs}_x(\text{MA}_{0.17}\text{FA}_{0.83})_{1-x}\text{Pb}_{1-y}\text{Sn}_y(\text{I}_{0.83}\text{Br}_{0.17})_3$ active layers.

While the lattice parameters decreased slightly from pure Pb to pure Sn for all fixed Cs compositions, all Pb-Sn alloys exhibited larger lattice parameters than the pure Pb or Sn perovskites with dips at the 50% Sn (Fig. 2b). This nonlinear deviation is consistent for all Cs compositions. McGehee and co-workers reported slight nonlinear deviations of lattice parameters for $\text{Cs}_y\text{FA}_{1-y}\text{Pb}_x\text{Sn}_{1-x}\text{I}_3$ perovskites. This could be due to the nonlinear Pb-X-Sn bond resulted from octahedral tilting which creates a nonlinear lattice effect for Pb-Sn alloyed perovskites during the incorporation of more Sn. However, the trends are different. For example, our $\text{Cs}_x\text{Sn}_{25}$ perovskites have larger lattice parameters than those of Cs_xSn_0 perovskites while the lattice parameter of $\text{FAPb}_{0.75}\text{Sn}_{0.25}\text{I}_3$ perovskite is smaller than that of FAPbI_3 perovskite.⁴⁸ The opposite trend could be attributed to the smaller lattice parameters of Cs_xSn_0 in the range of 6.26-6.23 Å (Fig. 2b) compared to $\text{Cs}_y\text{FA}_{1-y}\text{Pb}_{0.75}\text{Sn}_{0.25}\text{I}_3$ in the range of 6.39-6.33 Å due to the introduction of the smaller MA^+ and Br^- . The smaller overall lattice parameter in our perovskites could make the octahedral tilting resulted nonlinearity of mixed Pb-X-Sn bond more prominent, allowing certain Pb-Sn alloyed perovskites to have a larger lattice parameter than pure Pb or Sn perovskites.

In addition, it was noticed that the full width at half max (FWHM) of the (100) peak becomes narrower with Sn addition when compared to the pure Pb perovskites (Fig. S2), indicating the high crystallinity of the 25-75% Sn perovskites, which is consistent with the grain growth shown in the SEM images in Fig. 1. Fig. 2c shows the intensity ratio of (110) and (100) peaks for all composition perovskites, illustrating the decrease in (110) peak intensity with addition Sn. For 75% and 100% Sn

Photoluminescence (PL) measurements were, therefore, performed with samples sealed in vacuum to better define the band gap trend (Fig. S3d). The band gaps estimated from the onsets of the absorption spectra (0-75% Sn compositions) and PL spectra (100% Sn composition) are graphed as a function of Sn composition for different Cs contents (Fig. 3a). For each fixed Cs composition, the band gaps decrease from the maxima around 1.57-1.61 eV of the pure Pb perovskites to the minima around 1.28 – 1.30 eV of the perovskites with 75% Sn and then increase to 1.47-1.52 eV for 100% Sn. The addition of Cs, however, causes two trends in band gap depending on Sn composition and the cross-over occurs at 50% Sn. The band gaps increase with the increase of Cs for Pb-rich perovskites while they decrease with the increase of Cs for Sn-rich perovskites. All these trends are mainly due to the influence of the M-X overlap and the A-site induced MX_6 octahedral tilting on the conduction and valence band edges of perovskites. First-principle electronic structure calculations have determined the conduction band minimum of metal halide perovskites is a hybrid of metal p and halide p orbitals with nonbonding character and the valence band maximum is an antibonding hybrid of metal s and halide p orbitals.⁴⁹ Changes in the M-X overlap, therefore, raise the energy of the valence band more directly while the conduction band, having less orbital overlap, responds less strongly to lattice distortions, allowing the band gap to decrease with increased M-X overlap. Although the Sn-X-Sn bond increases the orbital overlap compared to the Pb-X-Pb bond, the mixed Pb-X-Sn bonds allow for spin-orbital coupling and the least distorted, more linear Pb-X-Sn bond angles, resulting in the minimum band gaps at 75% Sn. The minimum band gaps at 75% Sn observed in

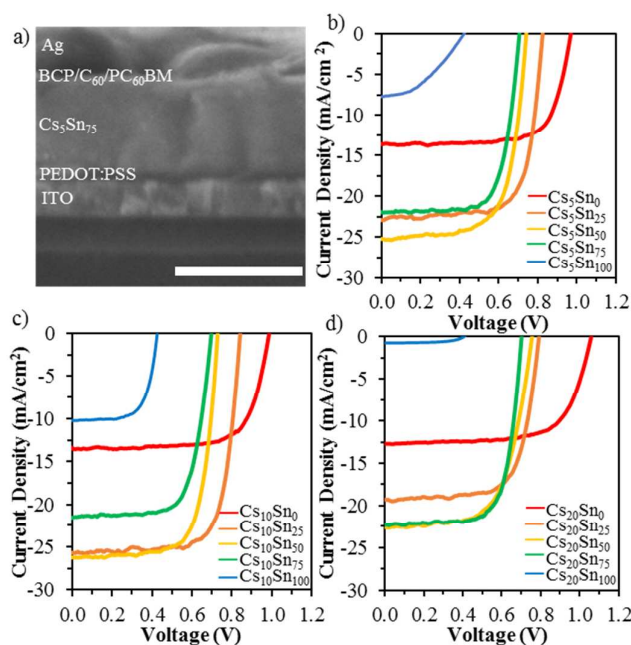


Fig. 4. (a) Cross-section SEM image showing the $\text{Cs}_{0.05}(\text{MA}_{0.17}\text{FA}_{0.83})_{0.95}\text{Pb}_{0.25}\text{Sn}_{0.75}(\text{I}_{0.83}\text{Br}_{0.17})_3$ PVSC with the following layers: ITO (~200 nm)/PEDOT:PSS (~50 nm)/perovskite (~450 nm)/PC₆₀BM/C₆₀ (20 nm)/BCP (8 nm)/Ag (150 nm). The current density-voltage (J-V) characteristics of $\text{Cs}_x(\text{MA}_{0.17}\text{FA}_{0.83})_{1-x}\text{Pb}_{1-y}\text{Sn}_y(\text{I}_{0.83}\text{Br}_{0.17})_3$ PVSCs with (b) $x = 0.05$, (c) $x = 0.10$, and (d) $x = 0.20$ with $y = 0, 0.25, 0.50, 0.75$, and 1.0 for each x under AM 1.5 illumination at a scan rate of 0.01 V s^{-1} from 0 to 1.2 V .

this work for triple cation, double halide Pb-Sn perovskites follow the same trend for single cation, single halide $\text{MAPb}_x\text{Sn}_{1-x}\text{I}_3$ perovskites.²⁶ The opposite trend of band gap change on Sn composition was also observed in $\text{FA}_{1-x}\text{Cs}_x\text{Pb}_{1-y}\text{Sn}_y\text{I}_3$ perovskites, where x ranged from 0 to 30% and y ranged from 0 to 100% .⁴⁸ A smaller A-site cation could increase the MX_6 octahedra tilting, which would increase the band gap, or contract the crystal lattice isotropically, which would decrease the band gap.⁴⁸ The pure Pb and Pb-rich perovskites follow a blue shift in band gap with increased Cs in the A-site, which is predominantly due to the MX_6 tilting decreasing M-X overlap, lowering the valence band. The pure Sn and Sn-rich perovskites follow the opposite, red shift in band gap with increased Cs in the A-site, which is mainly due to the isotropical lattice constrictions, resulting in an increasing M-X overlap.^{48,50} Our results support these two mechanisms for A-site induced band gap changes in previous literature while also showing the shift in predominant mechanisms occurring at 50% Sn even for triple cation, double halide Pb-Sn perovskites.

The band gap trends of $\text{Cs}_x(\text{MA}_{0.17}\text{FA}_{0.83})_{1-x}\text{Pb}_{1-y}\text{Sn}_y(\text{I}_{0.83}\text{Br}_{0.17})_3$ perovskites determined from UV-Vis and PL were also shown in the external quantum efficiency (EQE) spectra of PVSCs made with these films. As shown in Fig. 3b, fixed Cs with increasing Sn results in a red shift in EQE edges from 0% - 75% Sn. With fixed Sn and increasing Cs, there is a blue shift in EQE edge for Sn₀ and Sn₂₅ and no change for Sn₅₀, while a red shift for Sn₇₅.

To determine the viability of these films as solar cell active layers, PVSCs were fabricated using $\text{Cs}_x(\text{MA}_{0.17}\text{FA}_{0.83})_{1-x}\text{Pb}_{1-y}\text{Sn}_y(\text{I}_{0.83}\text{Br}_{0.17})_3$ as the active layer with the inverted perovskite

architecture of ITO/PEDOT:PSS/Perovskite/PC₆₀BM/C₆₀/BCP/Ag as shown in the cross-section SEM image in Fig. 4a. PEDOT:PSS acts as the solution processable hole transport layer (HTL) sandwiching the perovskite layer with the spin-coated electron transport layer (ETL) PC₆₀BM, which is commonly used to fill gaps in the perovskite layer, reducing surface roughness and passivating possible traps.⁵¹ The thermally deposited C₆₀ layer acts as a second ETL to improve band energy alignment and the BCP layer acts as a hole blocking layer (HBL) to increase charge separation and minimize recombination. Although the common device architecture for Sn-based PVSCs has the configuration of mesoporous TiO₂/Perovskite/spiro-OMeTAD/Au, the spiro-OMeTAD HTL uses dopants such as lithium bis(trifluoromethylsulfonyl)imide salt and 4-tert-butylpyridine to better align the spiro-OMeTAD work function with the active layer, facilitating hole extraction. These dopants have been shown to be reactive and introduce further instability to Sn-based perovskites in inert conditions.⁶ The use of mesoporous TiO₂ as an ETL also requires a high sintering temperature, which is unideal for mass manufacturing. The low temperature fabrication of the inverted structural PVSCs allows for adaptation to roll-to-roll processing, lowering manufacturing costs, improving intrinsic device stability, and lowering current density-voltage (J-V) hysteresis.⁵²

The photocurrent density-voltage (J-V) characteristics of fabricated PVSCs are shown in Fig. 4b-d with detailed photovoltaic parameters summarized in Table 1. To determine the effects of Sn additives, pure Pb PVSCs were fabricated as a control for the three Cs compositions. The open-circuit voltage (V_{oc}), short-circuit current density (J_{sc}), fill factor (FF) and PCE as

Table 1. Photovoltaic parameters of $\text{Cs}_x(\text{MA}_{0.17}\text{FA}_{0.83})_{1-x}\text{Pb}_{1-y}\text{Sn}_y(\text{I}_{0.83}\text{Br}_{0.17})_3$ PVSCs measured under AM 1.5 illumination obtained from forward J-V measurements.

Device	V_{oc} (V)	J_{sc} (mA cm^{-2})	FF	PCE (%)	PCE_{max}
Cs_5Sn_0	0.98 ± 0.01	12.55 ± 1.03	0.70 ± 0.03	8.61 ± 0.75	9.54
$\text{Cs}_5\text{Sn}_{25}$	0.82 ± 0	20.98 ± 1.35	0.71 ± 0.01	12.29 ± 0.52	13.45
$\text{Cs}_5\text{Sn}_{50}$	0.73 ± 0.01	21.60 ± 2.09	0.67 ± 0.01	10.66 ± 1.19	12.71
$\text{Cs}_5\text{Sn}_{75}$	0.74 ± 0.01	14.65 ± 1.73	0.66 ± 0.03	7.18 ± 1.22	8.41
$\text{Cs}_5\text{Sn}_{100}$	0.43 ± 0.01	5.67 ± 2.97	0.52 ± 0.07	1.30 ± 0.80	1.87
$\text{Cs}_{10}\text{Sn}_0$	0.98 ± 0.01	12.37 ± 0.76	0.69 ± 0.03	8.46 ± 0.79	9.56
$\text{Cs}_{10}\text{Sn}_{25}$	0.83 ± 0.01	22.39 ± 2.62	0.73 ± 0.01	13.54 ± 1.74	15.78
$\text{Cs}_{10}\text{Sn}_{50}$	0.72 ± 0.01	23.14 ± 2.69	0.65 ± 0.08	10.91 ± 2.60	13.52
$\text{Cs}_{10}\text{Sn}_{75}$	0.62 ± 0.01	23.15 ± 2.47	0.62 ± 0.04	8.87 ± 0.62	9.61
$\text{Cs}_{10}\text{Sn}_{100}$	0.41 ± 0.00	8.98 ± 1.39	0.65 ± 0.02	2.43 ± 0.45	2.81
$\text{Cs}_{20}\text{Sn}_0$	1.04 ± 0.03	11.85 ± 0.92	0.64 ± 0.04	7.92 ± 1.29	9.23
$\text{Cs}_{20}\text{Sn}_{25}$	0.78 ± 0.01	17.50 ± 1.16	0.69 ± 0.01	9.36 ± 0.60	10.56
$\text{Cs}_{20}\text{Sn}_{50}$	0.75 ± 0.01	22.07 ± 1.50	0.61 ± 0.04	9.99 ± 0.66	10.81
$\text{Cs}_{20}\text{Sn}_{75}$	0.61 ± 0	19.54 ± 0.71	0.61 ± 0.07	7.26 ± 0.71	8.11
$\text{Cs}_{20}\text{Sn}_{100}$	0.39 ± 0.03	1.34 ± 0.04	0.41 ± 0.05	0.21 ± 0.04	0.25

a function of Sn composition for different Cs contents were plotted in Fig. S4a-d, respectively. The average V_{oc} 's decrease from ~ 1.0 V to ~ 0.4 V with increased Sn from 0 to 100% for all three Cs contents, which has been previously attributed to mismatched energy levels from valence decrease in band gaps from 1.57-1.61 to ~ 1.32 eV (Fig. 3a). The smaller band gaps allow for an increased photo-response in the near infrared region as demonstrated in EQE spectra in Fig. 3b. Further increasing Sn to 75 and 100%, different Cs contents PVSCs exhibited different trends. The J_{sc} of $\text{Cs}_5\text{Sn}_{75}$ was maintained around 21 mA cm^{-2} because of both low band gap (~ 1.3 eV) (Fig. 3a) and high-quality film (Fig. S1). For $\text{Cs}_5\text{Sn}_{100}$, the J_{sc} decreased to 5.67 mA cm^{-2} due to the introduction of large pinholes plus decreased crystallinity of the $\text{Cs}_5\text{Sn}_{100}$ perovskite film shown in Fig. S1. For $\text{Cs}_{20}\text{Sn}_{75}$, the J_{sc} was decreased slightly to the still reasonable level of 20 mA cm^{-2} most likely due to the introduction of small numbers of pinholes (Fig. S1). A significant decrease of J_{sc} to 8.98 mA cm^{-2} was observed for $\text{Cs}_{10}\text{Sn}_{100}$, which could be due to the band gap increasing (~ 1.44 eV) (Fig. 3a) and the small particles around grain boundaries resulted from phase segregations (Fig. S1). The overall improvement in J_{sc} demonstrates the beneficial role of Cs in improving crystallinity and film formation. The $\text{Cs}_{20}\text{Sn}_{100}$ PVSCs exhibited the lowest J_{sc} of 1.34 mA cm^{-2} , indicating the necessity for specified Cs tuning to optimize film formation and J_{sc} . Regardless of Cs content, FFs showed minimal variations for different Sn compositions. Combined with all parameters, the $\text{Cs}_{10}\text{Sn}_y$ PVSCs have the highest maximum PCE for each Sn composition. The $\text{Cs}_{10}\text{Sn}_{25}$ and $\text{Cs}_5\text{Sn}_{75}$ PVSCs currently hold the record high maximum PCE, 15.78 and 11.05%, respectively, for all reported PVSCs with 25 and 75% Sn compositions and architectures. The PVSCs with 75% Sn and all three Cs contents ($\text{Cs}_5\text{Sn}_{75}$, $\text{Cs}_{10}\text{Sn}_{75}$ and $\text{Cs}_{20}\text{Sn}_{75}$) exhibited the maximum PCE of 11.05, 10.45, 11.01%, respectively, all surpassing the PCE record holder for 75% Sn (7.8% with $\text{FA}_{0.8}\text{Cs}_{0.2}\text{Sn}_{0.75}\text{Pb}_{0.25}\text{I}_3$)⁵³ and nearby 80% Sn (7.07% with $\text{MAPb}_{0.2}\text{Sn}_{0.8}\text{I}_3$)⁵⁶. This could be due to the higher V_{oc} with the V_{oc} averages of 0.71, 0.68 and 0.70 V for $\text{Cs}_5\text{Sn}_{75}$, $\text{Cs}_{10}\text{Sn}_{75}$ and $\text{Cs}_{20}\text{Sn}_{75}$, respectively, demonstrating that composition tuning through triple cation and double halide mixtures might improve band energy alignment in the inverted architecture. Although

Graetzel and co-workers demonstrated a higher PCE for the respective $\text{Cs}_{0.05}(\text{MA}_{0.17}\text{FA}_{0.83})_{0.95}\text{Pb}(\text{I}_{0.83}\text{Br}_{0.17})_3$ (Cs_5Sn_0) and $\text{Cs}_{0.1}(\text{MA}_{0.17}\text{FA}_{0.83})_{0.9}\text{Pb}(\text{I}_{0.83}\text{Br}_{0.17})_3$ ($\text{Cs}_{10}\text{Sn}_0$) devices, the TiO_2 solar architecture allows for a higher average V_{oc} of 1.13 V as well as improved FF and J_{sc} .² Liang and co-workers reported a similar inverted PEDOT:PSS architecture and toluene anti-solvent wash method resulting in photovoltaic parameters for the maximum forward scan of $\text{Cs}_{10}(\text{MA}_{0.17}\text{FA}_{0.83})_{90}\text{Pb}(\text{I}_{0.83}\text{Br}_{0.17})_3$ devices (PCE = 9.51%, V_{oc} = 0.94 V, FF = 0.53, J_{sc} = 16.95 mA cm^{-2}), which are comparable to our best performance $\text{Cs}_{10}\text{Sn}_0$ device (PCE = 9.56%, V_{oc} = 0.99 V, FF = 0.72, J_{sc} = 13.42 mA cm^{-2}),

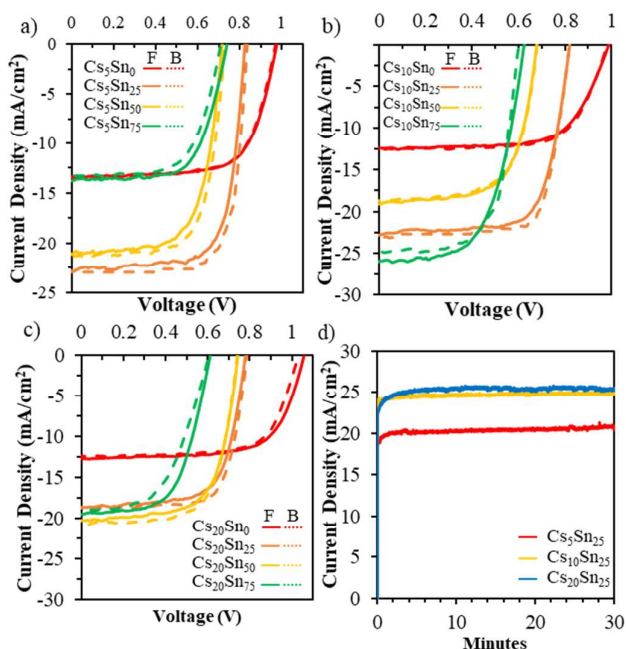


Fig. 5. Forward and backward scans of the J-V characteristics of $\text{Cs}_x(\text{MA}_{0.17}\text{FA}_{0.83})_{1-x}\text{Pb}_{1-y}\text{Sn}_y(\text{I}_{0.83}\text{Br}_{0.17})_3$ PVSCs at a scan rate of 0.01 V s^{-1} under AM 1.5 illumination: (a) $x = 0.05$, (b) $x = 0.10$, and (c) $x = 0.20$ with $y = 0, 0.25, 0.50, 0.75$, and 1.0 for each x . F indicates forward scan from 0 to 1.2 V and B indicates backward scan from 1.2 to 0 V. (d) The steady-state photocurrent measurements for $\text{Cs}_x(\text{MA}_{0.17}\text{FA}_{0.83})_{1-x}\text{Pb}_{0.75}\text{Sn}_{0.25}(\text{I}_{0.83}\text{Br}_{0.17})_3$ PVSCs with $x = 0.05, 0.10$, and 0.20 .

demonstrating the reproducibility of the anti-solvent wash method for our controls as we fabricated new compositions with Sn. It is worth noting that further PCE improvements of all high and pure Sn PVSCs can be achieved with further film optimization to remove pinholes and increase phase purity and crystallinity.

The hysteresis in J-V characteristics has been previously observed in PVSCs and has been attributed to a number of factors such as slow dynamic processing from trapping and detrapping of charge carriers, ferroelectric properties of perovskites, and ion migration.^{54,55} To determine the intrinsic hysteresis and device stability, the forward/backward J-V scans and the measurements of photocurrent stability at the maximum power were performed. As shown in Fig. 5a-c, forward and backward scans exhibited negligible hysteresis for almost all Sn

and Cs composition PVSCs. The pure Pb compositions had complete overlap for the forward and backward scans for 5% and 10% Cs. 25% and 50% Sn also had stable scans except for 20% Cs. The noticeable hysteresis in $\text{Cs}_{20}\text{Sn}_{75}$ could be attributed to the small pinholes introduced to the film morphology, which could increase trapping charge carriers. As shown in Fig. 5d of the photocurrent versus time at the maximum power, the $\text{Cs}_x\text{Sn}_{25}$ PVSCs, which had the highest performance parameters, remained stable under illumination in an inert atmosphere within the 30 min test period.

which can be attributed to the SnF_2 segregation. Although the XRD (Fig. S7) and SEM images (Fig. S8) were taken from the perovskite films that were air exposed for 10 days, which may have exacerbated the segregation/degradation process, there could still be some ion migration in the active layers of the PVSCs in the inert condition that affected the J_{sc} over 30 days. Sn containing PVSCs stored in the inert condition all maintained 80% of the original PCE. The $\text{Cs}_5\text{Sn}_{75}$, $\text{Cs}_5\text{Sn}_{50}$, $\text{Cs}_{10}\text{Sn}_{50}$, $\text{Cs}_{20}\text{Sn}_{25}$, and $\text{Cs}_{20}\text{Sn}_{50}$ PVSCs all had an increase in PCE overtime and finished the 30-day period with a normalized PCE at 1 or higher.

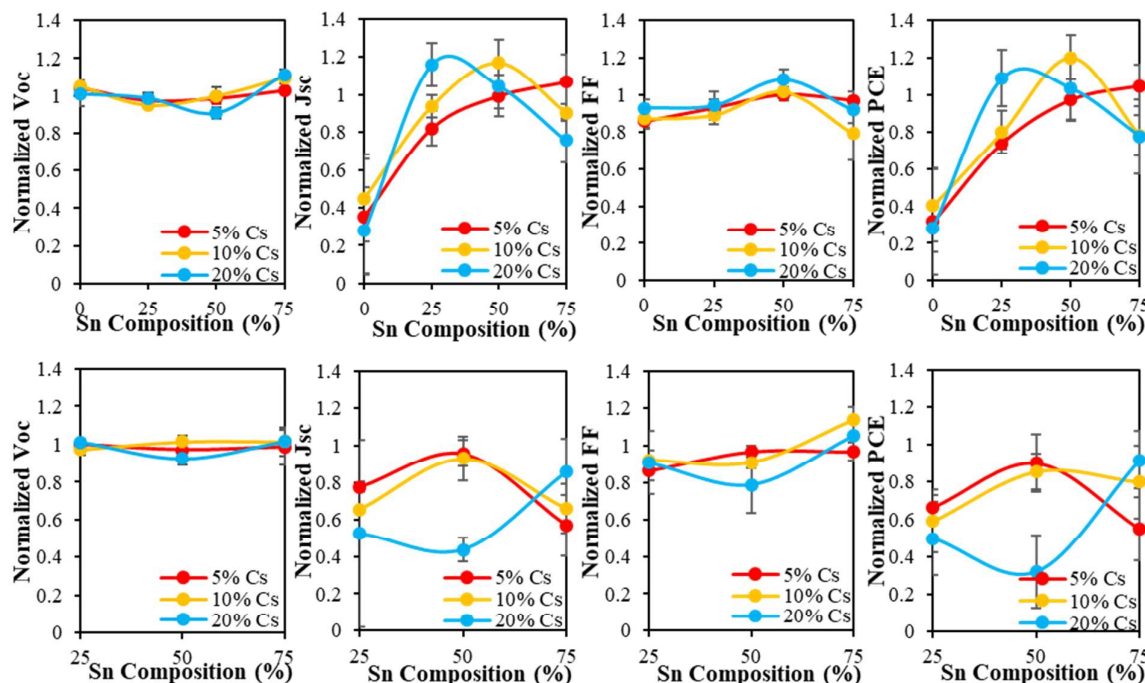


Fig. 6. Normalized (a, e) V_{oc} , (b, f) J_{sc} , (c, g) FF, and (d, h) PCE for unencapsulated PVSCs as a function of Sn composition for each Cs under inert conditions after 30 days (a, b, c and d) and after additional 5 days under ambient conditions (e, f, g and h).

A critical issue for Sn-based PVSCs is the ambient environment instability caused by the oxidation of Sn^{2+} to Sn^{4+} and degradation in humidity. To understand the effects of the various Cs compositions on the stability of Pb-Sn PVSCs, the long-term device stability in inert and ambient conditions were evaluated. Fig. S5 and S6 show the device performance of PVSCs over 30 days under the inert condition (glove box, $\text{O}_2 < 10$ ppm, $\text{H}_2\text{O} < 10$ ppm) and after an additional 5 days in ambient condition, respectively. Fig. 6 characterizes the normalized V_{oc} , J_{sc} , FF and PCE for PVSCs as a function of Sn composition for each Cs content at the 30th day in inert and the 5th day in ambient conditions following the storage in the glove box for 30 days, comparing them to pristine devices. The 100% Sn PVSCs were omitted from stability tests due to their low performance in pristine conditions while the pure Pb PVSCs were omitted from the air exposure measurements due to its already degraded state after 30 days in the glove box. The V_{oc} of all PVSCs tested retained at least 87% of their original values in inert and ambient conditions demonstrating the stability of band energy alignments. Although there is fluctuation in FF values with air exposure, the biggest contributor to PCE degradation is the J_{sc} ,

We proposed that the SnF_2 enhanced phase segregation created highly conductive Sn, F, Br rich particles as shown in the energy dispersion spectroscopy (EDS) measurements (Fig. S9 and Table S1), temporarily increasing the J_{sc} before further segregation resulting in more recombination centers. All the devices were moved out of the glove box after 30 days and stored in ambient condition and tested. After leaving in ambient condition with $35 \pm 5\%$ humidity for 5 days, the $\text{Cs}_5\text{Sn}_{50}$, $\text{Cs}_{10}\text{Sn}_{50}$, $\text{Cs}_{10}\text{Sn}_{75}$ and $\text{Cs}_{20}\text{Sn}_{75}$ PVSCs can retain over 80% of the original PCE. The $\text{Cs}_5\text{Sn}_{50}$ and $\text{Cs}_{20}\text{Sn}_{75}$ PVSC retained 90 and 92% of the original PCEs, respectively, demonstrating that Cs can be used to improve the stability of high Sn PVSCs in ambient conditions.

Conclusions

In summary, for the first time the optimized triple cation Cs/FA/MA and double halide Br/I compositions were applied to Pb-Sn alloyed perovskites $\text{Cs}_x(\text{MA}_{0.17}\text{FA}_{0.83})_{1-x}\text{Pb}_{1-y}\text{Sn}_y(\text{I}_{0.83}\text{Br}_{0.17})_3$. The synthesized perovskite films were smooth, dense and showed pure cubic α -phase with a high crystallinity.

The MX₆ octahedral tilting and lattice constriction from the compositional tuning resulted in a nonlinear lattice trend for the Pb-Sn alloyed perovskites as well as the opposite band gap trends in the Pb-rich or Sn-rich perovskites with the increase of Cs for fixed Sn compositions. The corresponding devices achieved high efficiency on a PEDOT:PSS inverted architecture with a PCE_{max} of 15.78% for the Cs_{0.10}(MA_{0.17}FA_{0.83})_{0.90}Pb_{0.75}Sn_{0.25}(I_{0.83}Br_{0.17})₃ PVSC and a record high PCE_{max} of 11.05% for the high Sn Cs_{0.05}(MA_{0.17}FA_{0.83})_{0.95}Pb_{0.25}Sn_{0.75}(I_{0.83}Br_{0.17})₃ PVSC. Adding Cs to the triple cation Cs/MA/FA, mixed halide Br/I Pb-Sn alloyed perovskites suppressed yellow phase and Sn⁴⁺ impurities, creating highly uniform and crystalline perovskite films that can retain ~80% of their initial PCE for 30 days in the inert condition followed by 5 days in the ambient condition with a relatively humidity of 35 ± 5%. Overall, this study demonstrated the implementation of the triple cation, double halide as an effective strategy for improving performance and stability of high Sn PVSCs, providing a route towards lead-free devices in the future.

Experimental

Materials

Lead (II) iodide (PbI₂, 99%), tin (II) iodide (SnI₂, 99.99%), lead (II) bromide (PbBr₂, 99.999%), cesium iodide (CsI, 99.999%), tin (II) fluoride (SnF₂, 99%), toluene (anhydrous, 99.8%), chloroform (≥ 99.99%), γ-butyrolactone (GBL, ≥ 99%), N,N-dimethyl sulfoxide (DMSO, anhydrous, ≥ 99.9%), and bathocuproine (BCP, 96%) were purchased from Sigma-Aldrich (St. Louis, Missouri) without further purification. Methylammonium iodide (MAI), formamidinium iodide (FAI), and formamidinium bromide (FABr) were purchased from Greatcell Solar (Queanbeyan, Australia) without further purification. The PC₆₀BM (> 99.5%) and C₆₀ (> 99.5%) were purchased from American Dye Solar (Quebec, Canada).

Perovskite Thin Film Fabrication

The perovskite precursor solutions were made by dissolving MAI, FAI, PbI₂, PbBr₂, SnI₂, and FABr, at the corresponding molar ratios in GBL and DMSO (volume ratio 7:3) with a total concentration of 2.5 M. A 10% SnF₂ per molar weight of SnI₂ was added in the precursor solution as a reducing agent. CsI was dissolved in DMSO at a concentration of 1.5 M and added to the precursor to achieve the correct triple cation composition. The precursors were mixed at 60 °C for 1 h and were filtered through a 0.2 μm PTFE filter before use. Plain glass was cut into 15 mm x 15 mm substrates, then were cleaned via ultrasonication for 15 min in detergent in Millipore deionized water, Millipore deionized water, acetone, and isopropanol in sequence. The substrates were treated with oxygen plasma under 100 W for 10 min. A 70 μL drop of precursor solution was spin-coated on a cleaned glass substrate at 500 rpm for 5 s, 1000 rpm for 15 s, and 4000 rpm for 40 s in a nitrogen glove box. A toluene anti-solvent was *in situ* dripped onto the substrate during the last 15 s of the third spin-coating step. The volume of the anti-solvent was decreased from 800 to 700, 600, 500, and 400 μL for Cs_x(MA_{0.17}FA_{0.83})_{1-x}Pb_{1-y}Sn_y(I_{0.83}Br_{0.17})₃ perovskites with y = 0,

0.25, 0.5, 0.75 and 1.0, respectively. The perovskite films were then thermally annealed at 100 °C for 10 min.

Film Characterization

Scanning electron microscopy (SEM) and energy dispersion spectroscopy (EDS) were acquired using FEI Sirion SEM operated at 5 kV and 15 kV to gain surface morphology and elemental compositions of perovskite thin films, respectively. Two-dimensional X-Ray diffraction (XRD) patterns were collected with Bruker GADDS D8 Focus Powder Discover diffractometer using Cu Kα radiation (λ = 1.5419 Å) and the data was processed using the EVA package provided by Bruker Axs to investigate crystalline structures of perovskite thin films. Ultraviolet-visible (UV-Vis) absorption spectra were collected using a Varian Cary 5000 UV-Vis-NIR spectrophotometer. Photoluminescence (PL) spectra were obtained with a modified Horiba LabRAM HR-800 with 532 nm laser excitation and a Czerny–Turner monochromator blazed at 1200 nm. Measurements were conducted at 1 Sun above band gap equivalent photon flux with a 532 nm cw laser. The PL experiments were conducted in a N₂-filled KF flange with a borosilicate glass window.

Device Fabrication

ITO coated glass substrates (10 ohm/sq ITO, Colorado Concept Coatings LLC) were cut and cleaned as described above. The PEDOT:PSS (Al 4083, Heraeus Clevious™) solution was filtered with a 0.45 μm nylon filter. A 70 μL drop of PEDOT:PSS was spin-coated on a cleaned ITO coated glass substrate at 5000 rpm for 60 s and annealed at 150 °C for 10 min in air. The substrates were transferred to a glove box and the perovskite thin films were fabricated as described above. A PC₆₀BM solution (15 mg ml⁻¹ in chloroform) was then spin coated on the perovskites films at 4000 rpm for 60 s and dried without annealing. The substrates were loaded into a thermal evaporation chamber to thermally deposit 20 nm of C₆₀ and 8 nm of BCP. Finally, a mask with 3.14 x 10⁻⁶ m² area holes was placed on devices to evaporate 150 nm of silver for electrodes in a high vacuum evaporator (< 1 x 10⁻⁶ Torr). The resulting device structure is ITO/PEDOT:PSS/Perovskite/PC₆₀BM/C₆₀/BCP/Ag.

Device Characterization

The photocurrent density-voltage (J-V) curve measurements were conducted in a N₂ glovebox with a Keithley 2400 Source Meter and a Solar Light Co. Xenon lamp (16S-300W) and AM 1.5 filter. Before measurements, the light intensity was calibrated to 100 mW cm⁻² using a standardized National Renewable Energy Laboratory calibrated silicon solar cell. EQE measurements were performed in ambient conditions without encapsulation using a xenon lamp (Oriel, 450W) light source, a monochromator (Newport Cornerstone 130), optical chopper, lock-in amplifier (Stanford Research Corp SR830), and finally a NIST-certified Si-photodiode (Thorlabs FDS 100-CAL) for calibration.

Conflicts of interest

ARTICLE

Journal of Materials Chemistry A

The authors declare no conflict of interest.

Acknowledgements

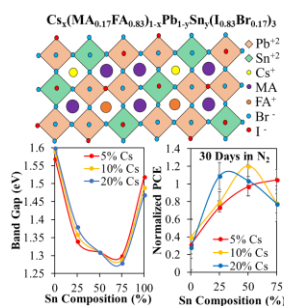
This work was supported by the National Science Foundation (NSF) (CBET-1748101 and CMMI-1661660). GAT acknowledges the support from the NSF Graduate Research Fellowships Program Fellowship and the University of Washington (UW) Clean Energy Institute (CEI) Graduate Research and Education Fellowships funded by the State of Washington via the Washington Research Foundation. Part of this work was conducted at the Molecular Analysis Facility, a National Nanotechnology Coordinated Infrastructure site at the UW which is supported in part by the NSF (ECC-1542101), the UW, the Molecular Engineering & Sciences Institute, the CEI, and the National Institutes of Health. Some device fabrications were carried out in the UW Department of Chemistry's Photonics Research Center. UV-Vis-NIR absorption measurements were carried out in the UW Department of Chemistry's Spectroscopic and Analytical Instrumentation facility. EQE and photoluminescence measurements were conducted in the labs of Professors Alex Jen and Hugh Hillhouse, respectively.

Notes and references

- A. Kojima, K. Teshima, Y. Shirai, T. Miyasaka, *J. Am. Chem. Soc.* 2009, **131**, 6050.
- M. Saliba, T. Matsui, J. Y. Seo, K. Domanski, J.P. Correa-Baena, M.K. Nazeeruddin, S.M. Zakeeruddin, W. Tress, A. Abate, A. Hagfeldt, M. Gratzel, *Energy & Env. Sci.*, 2016, **9**, 1989.
- M. Lee, H. Snaith, *Science Magazine*, 2012, **338**, 643.
- J.H. Heo, D.H. Song, S.H. Im, *Adv. Mater.*, 2014, **26**, 8179.
- P. Prajontat, T. Dittrich, *J. Phys. Chem. C*, 2015, **119**, 9926.
- F. Hao, C. C. Stoumpos, D. H. Cao, R. P. H. Chang, and M. G. Kanatzidis, *Nat. Photonics*, 2014, **8**, 489.
- S.D. Stranks, G.E. Eperon, G. Grancini, C. Menelaou, M.J.P. Alcocer, T. Leijtens, L.M. Hertz, A. Petrozza, H.J. Snaith, *Science Mag*, 2013, **342**, 341.
- A. Miyata, A. Mitioglu, P. Piochoccka, O. Portugall, J. T. W. Wang, S.D. Stranks, H.J. Snaith, R.J. Nicholas, *Nat. Photonics*, 2015, **11**, 582.
- C. Wehrenfennig, G.E. Eperon, M.B. Johnston, H.J. Snaith, L.M. Herz, *Adv. Mater.*, 2014, **26**, 1584.
- M. A. Green, A. Ho-Baillie, H. J. Snaith, *Nat. Photon-*, 2014, **8**, 506.
- B. Conings, J. Drijkoningen, N. Gauquelin, A. Babayigit, J. D'Haen, L. D'Olieslaeger, Aa. Ethirajan, J. Verbeeck, J. Manca, E. Mosconi, F. De Angelis, H.G. Boyen, *Adv. Energy Mater.*, 2015, **5**, 1.
- C. Stoumpos, C.D. Malliakas, M. Kanatzidis, *Inorganic Chemistry*, 2013, **52**, 9019.
- J. A. Christians, P. A. M. Herrera, and P. V. Kamat, *J. Am. Chem. Soc.*, 2015, **137**, 1530.
- R.L.Z. Hoyer, P. Schulz, L.T. Schelhas, A.M. Holder, K.H. Stone, J.D. Perkins, D. Vigil-Fowler, S. Siol, D.O. Scanlon, A. Zakutayeu, A. Walsh, I.C. Smith, B.C. Melot, R.C. Kurchin, Y. Wang, J. Shi, F.C. Marques, J.J. Berry, W. Tumas, S. Lany, V. Stevanovic, M.F. Toney, T. Buonassisi, *Chem. Mater.*, 2017, **29**, 1964.
- Z. Li, M. Yang, J.-S. Park, S.-H. Wei, J. J. Berry, and K. Zhu, *Chem. Mater.*, 2015, **28**, 284.
- G.E. Eperon, G.M. Paterno, R.J. Sutton, A. Zampetti, A.A. Haghighirad, F. Cacialli, H.J. Snaith, *J. Mater. Chem.*, 2014, **3**, 19688.
- R.J. Sutton, G.E. Eperon, L. Miranda, E.S. Parrott, B.A. Kamino, J.B. Patel, M.T. Horantner, M.B. Johnston, A.A. Haghighirad, D.T. Moore, H.J. Snaith, *Adv. Energy Mater.*, 2016, **6**, 1.
- D.P. McMeekin, G. Sadoughi, W. Rehman, G.E. Eperon, M. Saliba, M.T. Horantner, A. Haghighirad, N. Sakai, L. Korte, B. Rech, M.B. Johnston, L.M. Hertz, H.J. Snaith, 2016, **351**, 151.
- D. Bi, W. Tress, M.I. Dar, P. Gao, J. Luo, C. Renevier, K. Schenk, A. Abate, F. Giordano, J.P. Correa-Baena, J.D. Decoppet, S.M. Zakeeruddin, M.K. Nazeeruddin, M. Gratzel, A. Hagfeldt, *Sci. Adv.*, 2016, **2**, 1.
- M. Saliba, S. Orlandi, T. Matsui, S. Aghazada, M. Cavazzini, J.P. Correa-Baena, P. Gao, R. Scopelliti, E. Mosconi, K.H. Dahmen, F. De Angelis, A. Abate, A. Hagfeldt, G. Pozzi, M. Gratzel, M. K. Nazeeruddin, *Nat. Energy*, 2016, **1**, 1.
- Y. Wang, J. Wu, P. Zhang, D. Liu, T. Zhang, L. Ji, X. Gu, Z.D. Chen, S. Li, *Nano Energy*, 2017, **39**, 616.
- S. Chatterjee and A. J. Pal, *J. Mater. Chem.*, 2018, **6**, 3793.
- Q. Chen, N. De Marco, Y.M. Yang, T.B. Song, C.C. Chen, H. Zhao, Z. Hong, H. Zhou, Y. Yang, *Nano Today*, 2015, **10**, 355.
- X. Liu, Z. Yang, C.C. Chen, A. Rajagopal, S.T. Williams, Y. Sun, A.K.Y. Jen, *J. Mater. Chem.*, 2015, **4**, 17939.
- Y. Ogomi, A. Morita, S. Tsukamoto, T. Saitho, N. Fujikawa, G. Shen, T. Toyoda, K. Yoshino, S.S. Pandey, T. Ma, S. Hayase, *J. Phys. Chem. Lett.*, 2014, **5**, 1004.
- F. Hao, C.C. Stoumpos, R.P.H. Chang, M. G. Kanatzidis, *Journal of American Chemical Society*, 2014, **136**, 8094.
- Z. Yang, A. Rajagopal, A. K.-Y. Jen, *Adv. Mater.*, 2017, **29**, 1704418.
- K. Liang, D.B. Mitzi, M.T. Prikas, *Chem. Mater.*, 1998, **10**, 403.
- F. Hao, C.C. Stoumpos, P. Guo, N. Zhou, T.J. Marks, R.P.H. Chang, M.G. Kanatzidis, *J. Am. Chem. Soc.*, 2015, **137**, 11445.
- Z. Yang, A. Rajagopal, C.C. Chen, S.B. Jo, B. Liu, T. Zhao, A.K.Y. Jen, *Adv. Mater.*, 2016, **28**, 8990.
- A.G. Kontos, A. Kaltzoglou, E. Sirandi, D. Palles, G.K. Angeli, M.K. Arfanis, V. Psycharis, Y.S. Raptis, E.I. Kamitsos, P.N. Trikalitis, C.C. Stoumpos, M.G. Kanatzidis, P. Falaras, *Inorg. Chem.*, 2016, **56**, 84.
- I. Chung, B. Lee, J. He, R.P.H. Chang, M.G. Kanatzidis, *Nature*, 2012, **485**, 486.
- S.J. Lee, S.S. Shin, Y.C. Kim, D. Kim, T.K. Ahn, J.H. Noh, J. Seo, S.I. Seok, *J. Am. Chem. Soc.*, 2016, **138**, 3974.
- W. Liao, D. Zhao, Y. Yu, C.R. Grice, C. Wang, A.J. Cimaroli, P. Schulz, W. Meng, K. Zhu, R.G. Xiong, Y. Yan, *Adv. Mater.*, 2016, **28**, 9333.
- N. J. Jeon, J. H. Noh, Y. C. Kim, W. S. Yang, S. Ryu, and S. I. Seok, *Nat. Mater.*, 2014, **13**, 897.
- F. Hao, C.C. Stoumpos, P. Guo, N. Zhou, T.J. Marks, R.P.H. Chang, M.G. Kanatzidis, *J. Am. Chem. Soc.*, 2015, **137**, 11445.
- E. Zheng, B. Yuh, G. A. Tosado, and Q. Yu, *J. Mater. Chem. C*, 2016, **5**, 3796.
- L. Zhu, B. Yuh, S. Schoen, X. Li, M. Aldighaithir, B.J. Richardson, A. Alamer, Q. Yu, *Nanoscale*, 2015, **8**, 7621.
- F. Ma, J. Li, W. Li, N. Lin, L. Wang, and J. Qiao, *Chem. Sci.*, 2016, **8**, 800.
- J. Liang, C. Wang, P. Zhao, Z. Lu, Y. Ma, Z. Xu, Y. Wang, H. Zhu, Y. Hu, G. Zhu, L. Ma, Tao, Chen, Z. Tie, J. Liu, Z. Jin, *Nanoscale*, 2016, **9**, 11841.
- C. Yi, J. Luo, S. Meloni, A. Boziki, N. Ashari-Astani, C. Gratzel, S.M. Zakeeruddin, U. Rothlisberger, M. Gratzel, *Energy & Environ. Sci.*, 2015, **9**, 656.
- M. Deepa, M. Salado, L. Calio, S. Kazim, S. M. Shivaprasad, S. Ahmad, *Phys. Chem. Chem. Phys.*, 2016, **19**, 4069.
- V. Goldschmidt, *Naturwissenschaften*, 1926, **14**, 477.

- 44 G. Kieslich, S. Sun, and A. K. Cheetham, *Chem. Sci.*, 2014, **6**, 3430.
- 45 B. Saporov and D. B. Mitzi, *Chem. Rev.*, 2016, **116**, 4558.
- 46 W. Travis, E. N. K. Glover, H. Bronstein, D. O. Scanlon, and R. G. Palgrave, *Chem. Sci.*, 2015, **7**, 4548.
- 47 J.-W. Lee, D.-H. Kim, H.-S. Kim, S.-W. Seo, S. M. Cho, and N.-G. Park, *Adv. Energy Mater.*, 2015, **5**, 1501310.
- 48 R. Prasanna, A. Gold-Parker, T. Leijtens, B. Conings, A. Babayigit, H.G. Boyen, M.F. Toney, M.D. McGhee, *J. Am. Chem. Soc.*, 2017, **139**, 11117.
- 49 J.H. Lee, N.C. Bristowe, J.H. Lee, S.H. Lee, P.D. Bristowe, A.K. Cheetham, H.M. Jang, *Chem. Mater.*, 2016, **28**, 4259.
- 50 C. Ferrara, M. Patrini, A. Pisanu, P. Quadrelli, C. Milanese, C. Tealdi, L. Malavasi, *J. Mater. Chem.*, 2016, **5**, 9391.
- 51 Y. Shao, Z. Xiao, C. Bi, Y. Yuan, J. Huang, *Nat. Comm.* 2014, **1**.
- 52 Z. Xiao, C. Bi, Y. Shao, Q. Dong, Q. Wang, Y. Yuan, C. Wang, Y. Gao, J. Huang, *Energy Environ. Sci.*, 2013, **7**, 2619.
- 53 M. Konstantakou, T. Stergiopoulos, *J. Mater. Chem.*, 2016, **5**, 11518.
- 54 H.J. Snaith, A. Abate, J.M. Ball, G.E. Eperon, T. Leijtens, N.K. Noel, S.D. Stranks, J.T.W. Wang, K. Wojciechowski, W. Zhang, *J. Phys. Chem. Lett.*, 2014, **5**, 1511.
- 55 E.L. Unger, E.T. Hoke, C.D. Bailie, W.H. Nguyen, A.R. Bowring, T. Heumuller, M.G. Christoforo, M.D. McGhee, *Energy Environ. Sci.*, 2013, **7**, 3690.
- 56 M. M. Tavakoli, S. M. Zakeeruddin, M. Graetzel, Z. Fan, *Adv. Mater.*, 2018, **30**, 1705998

Table of Content Image



Cs_x(MA_{0.17}FA_{0.83})_{1-x}Pb_{1-y}Sn_y(I_{0.83}Br_{0.17})₃ perovskites with cubic-phase morphologies were deployed in solar cells, achieving high efficiencies and improved stability for high Sn-containing devices.